

22 Title: A catastrophic flowslide overridden on liquefied substrate: The 1983 Saleshan
23 landslide in China

24

25 Authors: Fanyu Zhang, Jianbing Peng, Xiugang Wu, Fazhen Pan, Yao Jiang, Chao Kang,
26 Weijiang Wu, Wenguo Ma

27

28 **Abstract:** A flowslide overriding liquefied substrate can vastly enhance its disaster
29 after failure initiation, due to rapid velocity and long-runout distance during landslides
30 mobilized into flows. It is crucial to provide improved understanding to the mechanism
31 of these catastrophic flowslides for hazard mitigation and risk assessment. This study
32 focuses on the Saleshan landslide of Gansu in China, which is a typically catastrophic
33 flowslide overrode a liquefied sand substrate. Geomorphologic and topographic maps
34 along with analysis of seismic signals confirm its dynamic features and mobilized
35 behaviors. ERT surveying detected abundant groundwater in the landslide, which is
36 fundamental to its rapid long-runout distance. Particle size distributions and triaxial
37 shear behaviors affirmed more readily liquefied behavior of superficial loess and
38 underlying alluvial sand than red soil sandwiched them. We also examined the
39 liquefaction susceptibility of the alluvial sand under loading impact at undrained and
40 drained conditions. The alluvial sand is readily liquefied in the undrained condition
41 while it is difficult at drained condition due to rapid water pore pressure dissipation.
42 The results showed that the landslide experienced a sudden transformation from slide
43 on the steep slope where it originated to flow on a nearly flat terrace with abundant

44 groundwater that it overrode. This transformation can be attributed to the liquefied
45 alluvial sand substrate enhancing the whole landslide body mobility. Along with recent,
46 similar findings from landslides worldwide, substrate liquefaction may present a
47 widespread, significant increase in landslide hazard and consequent mobility and our
48 study reveals conditions necessary for this phenomenon to occur.

49

50 **Keywords:** Catastrophic flowslide, liquified substrate, mobilized transformation,
51 Saleshan landslide, China

52

53 **1. Introduction**

54 Flowslide is generally catastrophic worldwide. This kind of flow-like landslides is
55 always characterized by rapid velocity and long-runout distance during landslides
56 mobilized into flows, as such they usually cause more catastrophic threats to people,
57 environment, and property. Hence, it is curial to understand the mobility of these
58 catastrophic flowslides to hazard mitigation and risk assessment.

59 Some studies have been conducted to gain understanding of rapid long-runout
60 flowslides, involving field evidences, numerical and physical simulations, and shear
61 tests, along with very few field monitoring (Hutchinson and Bhandari, 1971; Misfeldt
62 *et al.*, 1991; Evans *et al.*, 2001; Wang *et al.*, 2003; Hungr and Evans, 2004; Crosta *et al.*,
63 2009a; Poschinger and Kippel, 2009; Iverson *et al.*, 2011; Crosta *et al.*, 2015; Iverson
64 *et al.*, 2015; Collins and Reid, 2020). However, mechanisms resulting in flowslide
65 mobility remain in debate, but some basic information is relatively clear. These studies
66 showed that the catastrophic flowslides commonly occur a transformation from slide
67 to flow. Furthermore, the transformed progress generally involves an undrained
68 loading by overlying landslide mass, which is more prevalent in granular materials,
69 such as sand, silt, and debris, along the flow path (Hutchinson and Bhandari, 1971;
70 Wang *et al.*, 2003; Sassa and Wang, 2005). The liquefaction of the granular materials
71 is crucial to maintain rapid and long-runout landside mobility (Hutchinson and
72 Bhandari, 1971; Evans *et al.*, 2001; Take and Beddoe, 2014). Furthermore, the
73 liquefied substrates have been considered vital to the transformed landslide mobility
74 (Iverson *et al.*, 1997; Wang *et al.*, 2003; Iverson *et al.*, 2011). Nevertheless, Mangeney

75 (2011) argued that flow-like mobility could also occur in completely dry granular
76 materials due to the lack of cohesion. Essentially, the mobility depends finally on the
77 frictional or rheologic behaviors of sheared granular materials. Additionally, the
78 transformation progress occurs in a channeling flow path, but also on a nearly flat
79 surface. The former has been the focus of considerable research effort in recent years.
80 In comparison, only few studies examined the transformation during movement from
81 steep upper regions onto very flat slopes, focusing on the base liquefaction of the flat
82 flow path (Hutchinson and Bhandari, 1971; Take and Beddoe, 2014; Crosta *et al.*,
83 2015). The 2014 Oso landslide obtained widespread attention to the catastrophic
84 long-runout mobility on a nearly flat surface, due to the apparent presence of a
85 liquified substrate (Iverson *et al.*, 2015; Iverson and George, 2016; Wartman *et al.*,
86 2016; Aaron *et al.*, 2017; Stark *et al.*, 2017; Collins and Reid, 2020). However,
87 understanding the mobility of the flowslide on a nearly flat surface remains unclear,
88 as evidenced by the broad range of hypotheses proposed to explain the well-studied
89 Oso landslide's mobility.

90 Loess flowslides are among the most common of the flow-like landslides, as loess
91 is prone to liquefaction under even an unsaturated condition. Earthquake and rainfall,
92 along with irrigation, have become familiar triggers of the catastrophic loess flowslides
93 in China. Earthquake-induced loess flowslides generally have long-runout mobility if
94 shallow groundwater conditions are present, resulting in liquefied loess with high
95 pore-water pressure and low shear resistance (Ishihara *et al.*, 1990; Wang *et al.*, 2014).
96 Currently, rainfall and irrigation become more frequent triggers to the loess flowslides.

97 Many studies showed that infiltrated water elevates the groundwater, and cause the
98 loess liquefaction forming the loess flowslides (Derbyshire *et al.*, 2000; Zhang *et al.*,
99 2014; Zhuang and Peng, 2014; Peng *et al.*, 2015; Peng *et al.*, 2017a; Peng *et al.*, 2017b;
100 Zhang *et al.*, 2017; Zhang and Wang, 2018; Peng *et al.*, 2019). Visibly, water plays a
101 dominant role in the occurrence of the loess flowslides. These studies mentioned
102 above significantly improved our understanding of loess flowslides. Still, much of this
103 effort has been in their initiation and failure mechanisms, examining the liquefied
104 behavior of the loess. Some studies of the mobility of the loess flowslides focused on
105 numerical simulation and field evidence (Peng *et al.*, 2015; Zhang *et al.*, 2017; Kang *et al.*,
106 2018; Li *et al.*, 2019). Yet there still remains an urgent problem to understand the
107 mobilized mechanisms of a landslide from a slide on the steep upper slope that
108 transforms into a flow on a nearly flat terrace. Such slides frequently threatened the
109 residents and their properties, and also cause major ecological and environmental
110 problems.

111 This study aims to provide an improved understanding of the transformed
112 mechanism from slide to flow overridden on a liquified substrate. We study a
113 catastrophic flowside, i.e., the Saleshan landslide of Gansu in China, which killed . We
114 produced geomorphologic and topographic maps for analyzing the movement
115 features of the landslide using cartographic and GIS techniques. We performed
116 electrical resistivity tomography (ERT) to detect groundwater conditions on the
117 landslide body and the terrace. Furthermore, we examined the particle size
118 distributions and triaxial shear behaviors of loess, red soil, and alluvial sand from the

119 landslide deposited zones. We especially performed two loading impact tests on the
120 alluvial sand specimens under drained and undrained status. Finally, we discussed the
121 transformed mechanism of this kind of landslide from slide on steep slopes to flow on
122 gentle terraces, and compare the difference in the liquefied entrainment occurred in a
123 steep channel bed erosion along its flow path. Our findings afford some fundamental
124 knowledge to the mobility of this kind of flowslides overridden on a liquefied substrate,
125 and specific assistances for landslide hazard mitigation and risk assessment.

126

127 **2. Saleshan landslide background**

128 The Saleshan landslide is situated in Dongxiang County, Gansu Province, China
129 (Fig. 1a), and occurred on an afternoon at about 5:46 local time on 7 March 1983,
130 which caused 237 deaths and damage of the four villages. Hence, the Saleshan
131 landslide is among the most disastrous one in the Baxie River catchment, which has
132 hundreds of different types of loess landslides at various sizes (Fig. 1b). Following the
133 updated Varnes landslide classification system, Hungr *et al.* (2014) described the
134 Saleshan landslide as a flowslide, which is characterized by long runout distance
135 traveled across a nearly flat surface. Fig. 1 c and d present the panoramic views of the
136 Saleshan landslide in 1983 and 2015.

137

138 **2.1 Geological structures**

139 Fig. 2 shows the simplified stratigraphic and topographic section through the pre-
140 landslide topography and the Saleshan landslide along its main sliding direction. The

141 presented stratigraphic and topographic section is revised to the previous version from
142 Zhang and Wang (1984) and Zhang *et al.* (2002). The geological structures can be
143 referred to in the previous studies (Zhang and Wang, 1984; Zhang *et al.*, 2002).

144 To geological structures before failure (Fig. 2a), the stratigraphic section of the
145 Saleshan landslide include in descending order: (1) Late Pleistocene Lishi Loess (Q₂),
146 (2) Middle Pleistocene Malan Loess (Q₃), (3) Pliocene mudstone and Cobblestone (N₂),
147 (4) Quaternary alluvial sand and gravel, colluvial mudstone and loess (Q₄). The alluvial
148 sand and gravel is located on the first terrace. Moreover, the previous studies
149 speculated that the colluvial mudstone and loess is the deposition of a historical
150 landslide situated over the first terrace (Kang *et al.*, 2018). There are no folds and faults
151 in Saleshan landslide area, which exhibits a simple geologic structure (Zhang *et al.*,
152 2002). Nevertheless, there are two sets of dominant joints, in which the east-west set
153 is matched with cracks in the main scarp of Saleshan landslide (Zhang *et al.*, 2002).

154 To geological structures after failure (Fig. 2b), a simplified stratigraphic section
155 can be described as follow: (1) the displaced material of landslide body covered over
156 the alluvial sand and gravel on the first terrace; and (2) the alluvial layer overlies the
157 undisturbed mudstone bedrock. Zhang *et al.* (2002) considered that the alluvial sand
158 and gravel is undisturbed on the first terrace, while other authors argued that the
159 landslide ploughed or impacted the alluvial layer, leading to erosional liquefaction of
160 the substrate (Wang *et al.*, 1988; Kang *et al.*, 2018). It is interesting to note the life-
161 saving tree on the landslide. When the Saleshan landslide occurred, a person tightly
162 held the tree, moving about 960 m without any injures (Zhang *et al.*, 2002; Kang *et al.*,

163 2018).

164

165 **2.1 Geomorphologic characteristics**

166 The Saleshan landslide is located on the south facing side of a steep slope ridge
167 on the northern side of Baxie River. The geomorphologic characteristic change of the
168 Saleshan landslide mainly depends on the Baxie River terraces (Fig. 2). The elevation
169 of the Saleshan landslide ranges from 1950 m to 2280 m, including four terraces with
170 abrupt slope angle change. The top of the slope ridge is 2280 m elevation above the
171 fourth terrace, where the slope angle is larger than 50°. The fourth terrace is located
172 between 2195 m and 2080 m elevation, with a slope angle varying from 30° to 35°.
173 The third and second terraces have developed two gentle platforms, and their
174 elevation varies from 2080 m to 1970 m with a switched deep slope with an average
175 30° slope angle. The lowest first terrace is about 800 m away from the toe of the
176 Saleshan slope with nearly flat surface topography before slope failure. After the
177 Saleshan slope failure, the first terrace became the main accumulation zone. The
178 topographic change reveals that the Saleshan landslide failed from a deep upslope and
179 moved on a flat surface with easy liquified sand and gravel layer, which means an
180 abrupt transformation of movement style. This also indicates that the geologic
181 structure and geomorphologic characteristics is basic conditions for the long-runout
182 mobility during Saleshan landslide propagation.

183

184 **2.3 Hydroclimatic conditions**

185 The Baxie River basin is a semiarid climate environment. Commonly, the average
186 annual precipitation is 485 mm, with 80% of the total in the period from June to
187 September, and frequent rainstorms in summer (Zhang *et al.*, 2002; Kang *et al.*, 2018).
188 However, the climate presents a wetter environment since 1979, with annual
189 precipitation of 650 mm, and the winter precipitation in 1982 was also above average
190 reaching 66.3 mm (Zhang *et al.*, 2002). There has meltwater before failure in March
191 1983. Thus, the freeze-thaw effect was suggested to trigger the Saleshan landslide
192 (Huang, 2009). However, Kang *et al.* (2018) considered that the meltwater effectively
193 elevated groundwater, which would be attributed to progressive failure.

194 The groundwater is of phreatic water, which has all distributed below the fourth
195 terrace (Ma and Qian, 1998). Many springs overflow from the toe of the terraces on
196 both sides of the River valley. Notably, the shallow aquifer on the first terrace is known
197 from borehole information, and the depth of the groundwater table is about 2 m
198 below the ground surface (Ma and Qian, 1998). Besides, the storage water in the Jiuer
199 reservoir was used to the agricultural irrigation on the terraces, guaranteeing the long-
200 term shallow groundwater level. The groundwater information provides useful help to
201 understand the mobility of the Saleshan landslide.

202 Notably, no observed earthquake and rainfall was recorded in the Baxie River
203 basin in March 1983. Therefore long-term accumulated precipitation and irrigation,
204 rather than abrupt seismic shaking and rainfall infiltration, likely played a key role in
205 initiating the Saleshan landslide.

206

207 **3. Materials and methods**

208 **3.1 Geomorphological features mapping**

209 The geomorphological mapping provides geomorphologic characteristics as an
210 important aid for understanding the inherent problems on the propagation of the
211 landslide. For this purpose, we collected various data from old photos, field
212 investigations, remote images, previous references about Selanshan landslide, and
213 produced a graphical map of geomorphologic imprints using cartographic and GIS
214 techniques. The geomorphological map in this study is representative of many results
215 both from various published data and unpublished reports.

216

217 **3.2 Topographic changes detection**

218 The topographic change detection is a fundamental prerequisite for landslide
219 deposition thickness but also can provide a direct result assessment for landslide
220 numerical modeling. In this context, we first prepared two large scale topographic
221 maps at the scale of 1:10000 from before and after slope failure, and digitized the two
222 maps using ArcGIS software, and then constructed their digital elevation models
223 (DEMs). After which, we compared and analyzed the topographic change using the
224 Geomorphic Change Detection (GCD) 7.0 software (<http://gcd.riverscapes.xyz/>), which
225 is a powerful tool on geomorphological change detection (Wheaton *et al.*, 2010;
226 Wheaton *et al.*, 2015). The GCD produced DEM of Difference (DoD) maps before and
227 after the Saleshan landslide, and estimated the net change in geomorphologic features,
228 such as elevation, volume, area.

229

230 **3.3 Movement features analysis**

231 To analyze mobility after slope failure, we produce a map of movement features,
232 including motion displacement, motion direction, and motion velocity. The motion
233 displacement derives a direct estimate from the placemarks on landslide body,
234 including the sites from house and tree before and after failure. We also record the
235 motion direction of all the placemarks referred to the previous research results (Wang
236 *et al.*, 1988). We also calculated the motion velocity from displacement over time at
237 different sites of the Saleshan landslide. The mobility time derives from seismic signals
238 induced by Saleshan landslide at three seismic stations. The detailed procedure can
239 refer to the supplementary, involving how to digitize old analog seismograms to obtain
240 the relatively accurate time using a MATLAB™ toolbox of DigitSeis developed by
241 Bogiatzis (2015), with slight help of manual processing, to revitalize only three NS
242 analog seismograms from the three seismic stations (Supplementary note, Figs. 1 and
243 2).

244

245 **3.4 Textural and mechanical properties test**

246 To obtain the textural and mechanical properties, we taken disturbed loess and
247 red soil (product of mudstone) specimens close to the scarp of the Saleshan landslide,
248 as well as an alluvial sand specimen on the first terrace of Baxie River. These specimens
249 were oven-dried and disaggregated using a rubber hammer. We analyzed particle size
250 distributions of all the samples using a Microtrac S3500 laser diffraction instrument.

251 Each specimen tested eight times for consistency.

252 We conducted a series of consolidated undrained compression (CUC) triaxial tests
253 on all the three samples, and two quasi-dynamic impact stress loading (QSL) drained
254 and undrained triaxial tests on the alluvial sand samples. All the specimens have a
255 height of 10 cm and a diameter of 5 cm. All the examples were saturated by carbon
256 dioxide replacement, de-aired water flushing, and back pressure saturation. The
257 specimens were consolidated under a specified cell pressure and then compressed
258 under undrained conditions by means of the strain-controlled method. The axial strain
259 was increased at a rate of 0.01% per minute. The specimens were consolidated and
260 tested at cell pressures of 100, 200, 300 kPa. In CUC sets, compression at each cell
261 pressure was terminated when the axial strain close to 20%. In QSL sets, the specimens
262 were compressed by utilizing a sinusoidal stress loading module, but in which we used
263 a quarter loading period to load 160 kPa with 10 seconds at cell pressures of 200 kPa.
264 Notably, if the stress loading velocity is too rapid, this maybe generates a damage to
265 the triaxial apparatus. We performed one drained stress loading test, and other for the
266 undrained condition.

267

268 **3.5 Electrical resistivity survey**

269 To prospect the internal structure and hydrological environment of the Saleshan
270 landslide, we carried out four electrical resistivity tomography (ERT) profiles (see their
271 locations in Fig. 5) to obtain a detailed characterization about the electrical signals in
272 the first tens of meters below the ground surface. During the field survey, we used a

273 multielectrode system with 120 electrodes both in Wenner-Schlumberger and Wenner
274 arrays with an electrode spacing of 5 m. We located these electrical profiles using a
275 GPS and measured their topographic changes using a laser measuring technique.
276 Finally, we inverted the apparent resistivity data by a tomographic inversion technique
277 using the newest RES2DINV software. During the inversion, we implemented a
278 smoothness-type regularization constrained least squares by using incomplete Gauss-
279 Newton optimization technique, taking the topographical changes into account along
280 the profiles. The optimization technique is to iteratively adjust the resistivity to obtain
281 a minimal difference between the calculated and measured apparent resistivity values.
282 The absolute acceptable error provides a measurement of this difference.

283

284 **4. Results**

285 **4.1 Geomorphologic imprints**

286 The geomorphologic imprints on a landslide provide direct observation and
287 object analysis for dynamic features at different zones, but is important base to hazard
288 management land planning after the landslide. Fig. 3 shows the geomorphological
289 map of Saleshan landslide, which is a revised version based on the previous
290 conclusions (Zhang *et al.*, 2002; Wu and Wang, 2006). Our geomorphological map
291 presents an immediate and complete description of remaining features at different
292 locations throughout the landslide. From the viewpoint of space elements, we divide
293 the geomorphologic features into three styles. The dotted imprints only have spring
294 outcrop places. The linear features include zone boundaries, major and minor scarps,

295 various cracks, groundwater drainage, and surface water recharge. The planar features
296 involve depressions and hillocks in the zone of depletion, and grooves and hummocks
297 in the zone of accumulation, along with river gully and reservoir adjacent landslide.

298 There are several critical features worth analyzing. First, the different types of
299 cracks portray the deformation behaviors at respective locations. The cracks
300 distributed on the crown portray tensile deformation, and the lateral and transverse
301 cracks that occurred on the flank signify tractive deformation and fracturing process.
302 These radial cracks emerge thrust behavior on the toe. The depressions and hillocks
303 underwent extension and compression during the landslide movement. The significant
304 number of hummocks on the zone of accumulation show the evidence of fluidization
305 and extension during landslide mobility. There are more in the west-slide and central
306 regions than in the east slide in the zone of accumulation. Using hummocks that
307 explain the motion behavior of the fluidized landslides has also been paid special
308 attention by other authors (Paguican *et al.*, 2014; Collins and Reid, 2020; Dufresne and
309 Geertsema, 2020). The hummocks on a landslide can reveal important movement
310 features during their motion.

311 Fig. 4 shows the old photographs illustrating typical geomorphological imprints
312 of the Saleshan landslide. These photographs were taken shortly after the landslide in
313 1983. They not only well verify the evidence from the geomorphological map (Fig. 3),
314 but some of them provide more intuitive clues to uncover movement behavior. As
315 shown in Figs. 4c and 4d, the standing cow and life-saving tree reveal that the displaced
316 materials were incompletely disturbed, mainly maintaining the original stratigraphic

317 structure. Thus, we can speculate that the landslide body moved along a slip surface
318 with low shear resistance. Also, we observe differential movement on the zone of
319 accumulation, due to differences in disturbance and liquefaction of the displaced
320 materials (Fig. 4i-Fig. 4l). The loess at right flank is completely liquified (Fig. 4i), and
321 the deposit at the toe dammed the Baxie River gully with high water content (Fig. 4j).
322 While the deposit close to left flank buried the Jiuer reservoir (Fig. 4k), but they hold
323 some original structures presenting a low water content context.

324 From the geomorphologic imprints and evidence, we suggest that the Saleshan
325 landslide exists a motion transformation from slide to flow and that the flow-like
326 materials failed along a weak slip surface with some differences in deposit features.
327 Meanwhile, this evidence affords clues to analyze the characteristics of accumulation
328 and mobility after slope failure.

329

330 **4.2 Topographic changes**

331 There are few accurate measurements of the volume of a historical landslide,
332 because of a difficulty gaining the pre- and post-landslide topographic data. Fig. 5a
333 shows the elevation difference of the pre- and post-landslide on the Saleshan landslide.
334 Fig 5b and 5c show geomorphic change detection, the areal and volumetric elevation
335 change distributions. The negative elevation is for erosion, and positive elevation is for
336 accumulation, respectively. The elevation change range of erosion area is -142 to 0 m,
337 which located on the depletion zone. The elevation change range of accumulation
338 distributes between 0 and 39 m occurred in the accumulation zone. Volume

339 proportions of erosion and accumulation are almost the same, which are 55.69 and
340 44.31%, respectively. The decrease of accumulation volume may be due to the part of
341 loess flowing into Baxie river and Jieer reservoir. The areal proportion of erosion
342 (35.11%) is about half as much as deposition (64.89%).

343 To better detect the dynamic process of landslides, such as the change of area,
344 volume, and elevation in pre- and post-landslide, we used the Geomorphic Change
345 Detection (GCD) 7.0 software to construct seven two-dimensional profiles of the slip
346 surface in the movement direction and four profiles perpendicular to the movement
347 direction (Fig. 5a). By analyzing the profiles (Fig. 6), we can further understand the
348 characteristics of the topographic change of the Saleshan landslide. With steeper
349 slopes, the erosion probability is higher, and the maximum erosion height up to 139
350 meters, while the majority of accumulation occurs on the flat areas (P1-P7). It also can
351 be found that erosion mainly occurs on the fourth terrace, and the first terrace is the
352 accumulation zone. The accumulation and erosion features are related to the evidence
353 from geomorphologic characteristics. For the four profiles perpendicular to the
354 movement direction, the degree of erosion at area of P8 and P9 is much greater than
355 that of P10 and P11. As P8 and P9 is located at the trailing edge of the landslide, others
356 are at the leading edge of the landslide. Likewise, hillocks and scarps at the trailing
357 edge of the landslides are eroded, while gullies are piled up and filled. These profiles
358 describe the exterior morphological features and structures in the horizontal and
359 vertical directions, and it can highlight some changes in pre- and post-landslide.

360

361 4.3 Rapid and long-runout mobility

362 In the mobility of the rapid and long-runout landslides, its velocity, displacement,
363 and direction are vital kinematic parameters. Nevertheless, they are often uncertain
364 because this is practically difficult to identify the kinematic parameters accurately.
365 However, the surviving placemarks, e.g., tree and house, could be useful in the
366 dynamic analysis. Fig. 7 shows the motion displacement vector at different placemark
367 locations on the Saleshan landslide, and the calculated kinematic parameters are listed
368 in Table 1. Among these placemarks, there is the most significant motion displacement
369 of 1090 m and the highest motions velocity of 19.8 m/s. The results reveal that the
370 Saleshan landslide underwent rapid and long-runout mobility, in which appeared
371 apparent variable zonation of motion.

372 On the depletion zone, the three placemarks are almost the same with the
373 horizontal displacements from 310 to 340 m, which means that the vertical fall is
374 significant in the zone (see Fig. 1b). There has the lowest average velocity of 5.9 m/s
375 in the whole landslide zones with a velocity between 5.8 and 6.2 m/s. Due to the
376 calculated velocities on the total mobilized time of 55 seconds, the velocity of the
377 depletion zone may severely be underestimated in the three placemarks. The previous
378 dynamic studies and eyewitness account showed that the velocity of the sliding blocks
379 both exceeds 20 m/s in the depletion zone (Miao *et al.*, 2001; Zhang *et al.*, 2002; Kang
380 *et al.*, 2018).

381 On the accumulation zone, the displacement vectors present distinct kinematic
382 differences. The placemarks of the central accumulation zone have the greatest

383 motion displacement with the highest landslide velocities. There have relatively more
384 significant displacement and velocity on the west accumulation zone than on the east
385 accumulation zone. It should be noted that there have relatively low velocity and small
386 motion displacement closer to both the flanks. It is consistent with the field evidence
387 (Fig. 4k). This means that the displaced materials immediately stop after rupturing the
388 slide surface. In addition, the motion directions of the various placemarks depend on
389 the original topographic changes and geomorphologic features (Fig. 3 and Fig. 4).

390 In sum, the Saleshan landslide was rapid in the progress of long-distance motion.
391 The motion of Saleshan landslide primarily occurred on the accumulation zone, in
392 which the velocity and displacement of the displaced materials decrease from the
393 central zone to two flanks. The motion features are matched with the evidence from
394 geomorphologic maps and topographic changes (Fig. 3~Fig. 6). Besides, the
395 underestimated velocity derived from displacement and time may result in some
396 misleading to kinematic analysis.

397

398 **4.4 Structural and hydrological constraints**

399 ERT is widely used in landslide investigation characterized by a complex geological
400 setting (Perrone *et al.*, 2014). And recently time-lapse ERT is increasingly applied in
401 long-term landslide monitoring (Grandjean *et al.*, 2011; Chambers *et al.*, 2013;
402 Wilkinson *et al.*, 2016; Crawford *et al.*, 2019). Thus, ERT used as a conventional
403 geophysical prospecting method to the geological structure and hydrological
404 environment of a landslide, now becomes a convenient technology using in-situ

405 landslide monitoring.

406 Fig. 8 shows the interpreted Wenner ERT sections of four profiles on the Saleshan
407 landslide, and the detailed location of the four profiles are shown in the index figure
408 and Fig. 6. The profile L1 is longitudinal through the front zone of depletion, and the
409 end zone of accumulation along movement direction (Fig. 8a), and the profile C1 is
410 transverse through the toe region of rupture surface (Fig. 8b). In addition, the
411 interpreted Wenner Schlumberger ERT sections of four profiles are shown in
412 Supplementary Figs 3. The profiles L1 and C2 profiles orthogonally cross through the
413 middle zone of accumulation on the first terrace (Fig. 8c and d). In the profile L1, the
414 high resistivity sections correspond with the front zone of depletion with relatively low
415 water content and complete structure, while the end zone of accumulation presents
416 low resistivity. The information disclosed from ERT image is matched with the data of
417 borehole after the landslide (Wu and Wang, 2006), along with in-situ investigation.
418 Notably, there is an abundant phreatic region around the rupture surface. It can be
419 verified the evidence from the spring exposed on the third and fourth terrace, along
420 with the surface water convergence in the gully (See Fig. 3). The low resistivity in the
421 profile C1 is consistent with the gully sites, where there has high water content in
422 lowland causing thicker deposit and greater mobility (See Fig. 6). Meanwhile, the toe
423 zone of the rupture surface has relatively lower resistivity, comparing with the zone of
424 depletion. The information from profiles L1 and C2 shows that the displaced materials
425 thickness vary between 15 and 20 m, and that they deposited on the original ground
426 surface (Fig. 6). The deposit is thinner closer to the tip of the Saleshan landslide.

427 Notably, the sediments below the farmland ground exert a very low resistivity
428 signifying a high water content condition. This is well-matched with direct field
429 observations after the landslide, such as loess liquefaction and deposit with high water
430 content (see Fig 4j and Fig 4l) on the west zone of accumulation.

431 The electrical resistivity could obtain useful geophysical signals varying with the
432 nature and state of granular materials, as well as the fluid in the granular medium.
433 Thus, the four ERT survey images add information on the internal structure of the
434 Saleshan landslide, which is consistent with the geomorphologic features and
435 topographic changes. Meanwhile, the ERT images well provide the hydrological
436 information, which helps the understanding of the propagation of the Saleshan
437 landslide.

438

439 **4.5 Liquefaction behaviors**

440 **4.5.1 Particle size distribution**

441 The particle size distributions are often crucial for appraising liquefaction
442 potential of flow slides (Kramer, 1988; Picarelli, 2010), and could be indirectly used to
443 interpret liquefaction behaviors of fine granular soils. Fig. 9 shows the exemplified
444 particle size distribution of the three types of soil on the Saleshan landslides. To
445 facilitate a much clearer view of particle size, Fig. 9b uses a linear abscissa, rather than
446 a logarithmic abscissa. Other repeated test results were shown in Supplementary Figs.
447 4. The three samples are silty soils with uniform gradation. The loess has the greatest
448 fine fractions, and the alluvial sands include the coarsest fractions, whereas the red

449 soil is intermediate. Note that there are two modes on the frequency curves with two
450 unimodal curves and one bimodal curve. The loess and red soil have both a smooth
451 unimodal frequency distribution curve. The loess has a single fine component with a
452 size boundary of 20-60 μm and mean practice size (D_{50}) of 38 μm . The texture of the
453 red soil is like that of the loess, but it has a deviation with a size range of 25-55 μm ,
454 and a mean practice size of 43 μm . This kind of deviation may derive from the
455 modification of weathering processes of mudstone. The alluvial sand has a bimodal
456 frequency distribution of particle size, and the range is from 25 μm to 60 μm with a
457 mean practice size of 48 μm . Generally, the bimodal sand is a typical production of a
458 modern alluvial or fluvial environment (Taira and Scholle, 1979; Sun *et al.*, 2002).
459 Compared to evidence from the particle size distribution in other flowslides (Kramer,
460 1988; Picarelli, 2010; Zhang *et al.*, 2019), all the three samples on the Saleshan
461 landslide are characteristic of liquefaction features, which have the potential to liquefy
462 when close to saturation.

463

464 **4.5.2 Shear properties**

465 It is still necessary to examine the shear properties of soil to understand its
466 liquefaction behaviors directly. Fig. 10 compares the results of the undrained triaxial
467 shear tests of the three soils on the Saleshan landslide at the same confining pressure
468 (i.e., 200 kPa). Fig. 10a and b present the change deviator stress and pore water
469 pressure with axial strain. Fig. 10c depicts an effective stress path. The three specimens
470 have apparent differences in liquefaction behaviors. The loess specimen shows a

471 typical strain behavior maintaining high pore water pressure with an obvious decrease
472 in strength after peak value. The results are consistent with those observed in the
473 liquified or collapsed loess elsewhere (Zhang *et al.*, 2013; Wang *et al.*, 2014; Zhang *et*
474 *al.*, 2014; Zhang and Wang, 2018). This means that the loess in Saleshan landslide area
475 has visible liquefaction behavior under undrained condition, which is matched with in-
476 situ evidence (Fig. 4i). Notably, the red soil has the lowest liquefaction potential with
477 very light strength decrease after peak strength, although its particle size distribution
478 is located between loess and alluvial sand. It may be related to the strong cementation
479 or bonding existing in the weathering products of mudstone, which could attribute to
480 more clay fractions in the red soil. The alluvial sand specimen has the most significant
481 increase in pore water pressure after the peak strength. As shown in Fig. 9, the alluvial
482 sand is comprised of fine sand, and finer suspended muddy. The small amount of
483 suspended muddy slightly decreases the liquefaction of the alluvial sand. Similar
484 results have been found in ring shear and triaxial shear tests (Wang *et al.*, 2007;
485 Carraro *et al.*, 2009).

486 Fig. 11 shows the undrained triaxial test results for the alluvial sand specimens.
487 The deviator stress of all the specimens increases a peak value with increasing axial
488 strain; after that, abruptly decreases a steady-state with further increase in axial strain
489 (Fig. 11a). Meanwhile, the pore water pressure continuously increases to a steady
490 value with increasing axial strain (Fig. 11b). The effective stress paths show that pure
491 contractive behavior during undrained compression shearing (Fig. 11c). These results
492 further support that all the alluvial sand specimens present unusual liquefaction

493 behavior, and that is more prominent at low confining pressure.

494 Fig. 12 shows the triaxial test results from quasi-dynamic impact stress loading of
495 the alluvial sand specimens under drained and undrained conditions. In the drained
496 condition, the pore water pressure increases rapidly to 20 kPa in the progress of the
497 impact loading (i.e., 10s), and after that, it has an obvious decrease with almost
498 constant loading deviatoric stress of 160 kPa (Fig. 12a). Meanwhile, the generated pore
499 water pressure dissipated gradually with 100 s. The relatively high dissipation rate in
500 pore water pressure could be attributed to its inherent granular characteristics (Fig.9).
501 This is in contrast to the behavior exhibited in undrained impact loading, and the pore
502 water pressure is the same rapid increase as the drained impact stress loading (Fig.
503 12b). The desired impact stress could not fully load on the samples, and it has
504 completely collapsed with a rapid increase in pore water pressure. After that, the pore
505 water pressure slightly increases and, accordingly, a striking decrease in deviatoric
506 stress. It is essential for a structural collapse with a great axial displacement. The
507 results show that impact can generate pore water pressure on the alluvial sand, and
508 the undrained impact loading is easier to produce pore water pressure on the alluvial
509 sand than under drained conditions. Meanwhile, the quickly dissipated pore water
510 pressure on the alluvial sand may contribute to the liquefaction of the loess, and
511 consequently enhanced the mobility of the Saleshan landslide. This finding is
512 consistent with those research results from ring shear tests (Wang *et al.*, 2003) and
513 numerical simulation (Collins and Reid, 2020).

514

515 **4. Discussion**

516 **4.1 Transformation from a slide on the steep slope to flow on the gentle terrace**

517 The Saleshan landslide experienced a typical transformation from progressive
518 slide to catastrophic flow, i.e., velocity transition from slow to fast. The progressive
519 deformation along a sliding surface went through more than four years from the
520 evidence of monitoring data and eyewitness account, while the disastrous mobility
521 after failure initiation only underwent 60 seconds with about 1000 m mobility (Wang
522 *et al.*, 1988; Miao *et al.*, 2001; Zhang *et al.*, 2002; Wu and Wang, 2006; Kang *et al.*,
523 2018). Fig. 13 shows the hypothesized sequence from progressive deformation to the
524 catastrophic mobility of 1983 Saleshan landslide. The stage from slow to accelerated
525 deformation resulted in the pore water pressure accumulation in the toe zone of the
526 slope (Fig. 13a and b). After that, the landslides on dissected steep mudstone slope
527 transformed into a flow-type landslide that travels long runout distance across a nearly
528 flat terrace (Fig. 13c). Finally, the elevated reservoir water triggered landslide dam-
529 break (Fig. 13d). The previous studies have well analyzed the deformation mechanism
530 of the Saleshan landslide, but the unexpected flow-type mobility remains unclear. Thus,
531 we focus here on the transformation mechanisms from the slide on steep upper slope
532 to flow on nearly flat terrace.

533 The transformed landslide from slide to flow could be attributed to the unusual
534 structural and hydrological configurations of the toe and travel zone of the Saleshan
535 landslide. There is enough surface and sub-surface water convergence, leading to a
536 shallow groundwater level in alluvial sand layers with high liquefaction potential on

537 the first terrace. The evidence can prove the speculation from geomorphologic
538 mapping (Figs 2 and 3), ERT survey (Fig 8), and test results (Figs. 9-11). Generally, the
539 groundwater condition is key to the transformation from progressive slide to
540 catastrophic flow in the Saleshan landslide; meanwhile, the highly susceptible to
541 liquefaction alluvial sand is essential to the transformation. On the whole, the
542 transformation strictly depends on the liquefied substrate, i.e., alluvial saturated or
543 even partly saturated sand layer on the first terrace. Of course, as revealed by results
544 in field and laboratory (Figs. 3-5 and Fig. 10), the highly liquefied loess has a particular
545 contribution to the mobility after failure.

546 In the Chinese Loess Plateau, identical loess flowslides have frequently occurred
547 on the Jingyang platform (Xu *et al.*, 2009; Peng *et al.*, 2017a; Peng *et al.*, 2018; Li *et al.*,
548 2019). These researchers also proved that the hydrogeological conditions on the
549 nearly flat river terrace close to the current Wei River, i.e., the alluvial sand layer and
550 high groundwater level, control the transformed progress. Incorporating with
551 evidences from liquefied sand pipes observed in loess deposits (Xu *et al.*, 2009)
552 deduced a conceptualized liquefaction model in double layers (i.e., sand and loess)
553 along sliding surface on the nearly flat terrace. Peng *et al.* (2018) excavated several big
554 exploratory trenches on the accumulation of the flowslides, and they found typical
555 liquefied evidence of sand pipes and sand boils intruded into loess deposits. However,
556 it lacks direct ground evidence, which can be attributed to the thick loess deposits with
557 relatively low permeability. Also, the numerical simulation and shear wave detection
558 supported that liquefaction entrainment of the terrace sand deposits controls their

559 rapid and long runout mobility of those loess flowslides (Peng *et al.*, 2017a; Li *et al.*,
560 2019).

561 In the rest of the world, there have been similar structural and hydrologic
562 constraints with the above loess flowslides, which resulted in the same transformation
563 from slides on steep upper slope to flows with high mobility on a gentle lower terrace.
564 A famous example in Switzerland is the Flims rockslide avalanche, which liquefied
565 alluvial deposits on the terrace, leading to about 13 km displacement and damming of
566 the Vorderrhein river valley (Poschinger and Kippel, 2009). There was observed the
567 sub-vertical tubes of gravel composition almost without any fines in the landslide
568 deposits (Pavoni, 1968), and these finer materials such as sand and silt have been
569 washed out during water flow (Pavoni, 1968; Poschinger and Kippel, 2009). This is a
570 typical feature of liquefaction of alluvial deposits. The scholars in Czech Republic found
571 that a massive rockslide avalanche transformed as a long-runout landslide along the
572 terrace in the Bilina river (Burda *et al.*, 2018). The data shows that the slope of the
573 terrace is generally lower than 10 degrees in this study region (Poschinger and Kippel,
574 2009; Burda *et al.*, 2018). In Saskatchewan river, there have many landslides dissected
575 on shale slopes; some of them transformed into a fluidized landslide that mobilized far
576 beyond that expected on a nearly flat terrace. Moreover, multiples boreholes revealed
577 that the sliding surface is located on Tertiary sand in the Hepburn aquifer system
578 (Misfeldt *et al.*, 1991). Thus, enough groundwater and sand prone to liquefaction are
579 essential to these landslides that occurred in the Saskatchewan river region. Crosta *et*
580 *al.* (2015) presented multiple examples of landslides from steep slopes falling onto a

581 shallow erodible substrate or water layer, and then travel long-runout distance with
582 typical high velocity. Crosta and his colleagues have confirmed that the loading
583 processes of the overlying landslide mass resulted in the substrate liquefaction is key
584 to the mobility on a flat area (Crosta *et al.*, 2009a; Crosta *et al.*, 2009b; Crosta *et al.*,
585 2015; Crosta *et al.*, 2016). The very recent 2014 Oso landslide gained a lot of attentions
586 about its long runout mobility mechanism. The Oso landslide failed on steep slopes,
587 and then move along a nearly flat terrace (Iverson *et al.*, 2015; Iverson and George,
588 2016; Wartman *et al.*, 2016; Stark *et al.*, 2017; Collins and Reid, 2020). However, these
589 authors argue about the sequential stages of the Oso landslide and what material was
590 liquefied to explain its long runout mobility on the nearly flat alluvial plain.

591 The aforementioned typical examples improve our understanding of the
592 transformed landslide from slides on steep upper slopes to flow along gently terrace
593 and provide important insight of the base liquefaction of terrace deposits controlling
594 rapid and long-runout mobility, although disagreement remains regarding
595 mechanisms involved. However, these example landslides confirm that the unusual
596 structural and hydrologic configurations on the slope toe and fronted terrace zones
597 are critical for producing a rapid, long-runout landslide overriding terrace deposits.

598

599 **4.2 Rapid and long-runout mobility overridden on a liquefied substrate**

600 There should be similar transformed and mobilized mechanisms between
601 Saleshan landslide and these landslides mentioned above. The landslides detected on
602 steep upper slopes transformed into flow-type landslides, causing a rapid and long-

603 runout mobility overridden on the sand substrate on the nearly flat or gentle terrace
604 with enough water. Overall, there can divide into two stages after slope failure. One is
605 the instantaneous transformation of movement style at the toe of the slope; the
606 second is then long-runout mobility on the fronted terrace. They are both attributed
607 to dynamic loading from upper landslide mass on the lower liquefied substrate, which
608 is generally composed of alluvial sand and silt of terrace deposits. And consequentially,
609 the impact loading results in the generation of excess pore water pressure on the
610 liquefied sand at the toe of the terrace deposits under undrained condition, causing a
611 dramatic decrease in shear resistance of the saturated sand. Nevertheless, there has
612 an essential difference during transformation and mobility. The transformed moment
613 should be in an undrained condition with almost constant pore water pressure, along
614 with a lower shear resistance. While the mobilized progress is more like a drained
615 condition with almost constant shear resistance, comparing continuously dissipated
616 pore water pressure. Our triaxial dynamic impact loading provides a reasonable
617 explanation for the hypothesized mechanism to transformation and mobility (Figs. 12).
618 This mechanism is consistent with those obtained in physical and numerical
619 simulations performed by other authors (Take and Beddoe, 2014; Crosta et al., 2016;
620 Collins and Reid, 2020).

621 It is worth to mention another type of the transformed landslide from slide to
622 flow coupled with a channel bed erosion along its flow paths. In these events, the
623 displaced materials after failure entrain and liquefy saturated soil from its flow paths
624 along the channel on a slope (Evans *et al.*, 2001; Wang *et al.*, 2003; Hungr and Evans,

625 2004; Iverson *et al.*, 2011). There also had a typical case study in Chinese loess areas,
626 i.e., the Dagou loess flowslide with significant entrainment (Peng *et al.*, 2015; Zhang *et*
627 *al.*, 2017). The underlying process of entrainment and liquefaction is a rapid undrained
628 loading from the overriding landslide mass. As the dynamic undrained loading leads
629 to an increase in pore water pressure (Hutchinson and Bhandari, 1971; Sassa and
630 Wang, 2005; Wang *et al.*, 2013), and liquefy the underlying deposits on the channel
631 (Wang *et al.*, 2013; Collins and Reid, 2020), causing entrainment of landslide with
632 higher volume and greater mobility (Hungr and Evans, 2004). As the channelizing
633 topography can focus landslide momentum (Iverson *et al.*, 2015), and wet bed deposit
634 can enhance its mobilized capacity (Iverson *et al.*, 2011; Iverson *et al.*, 2015). In the
635 study to the 2014 Oso landslide, however, Iverson *et al.* (2015) pointed out that the
636 transformed landslide into a nearly flat surface is unlike virtually all the flow along the
637 channelling path. This is because, as suggested by Hutchinson and Bhandari (1971),
638 the rapid mobility overridden on a nearly flat slope partakes more of mass transport
639 than the mass movement.

640 Hence, the transformation from slide to flow includes two modes due to
641 topographic differences. However, there is the same increase in pore water pressure
642 in the liquefied substrate triggered by dynamic loading (Fig. 14). Meanwhile, the
643 transformation of the two movement types is both transients to the generation of pore
644 water pressure in the erosional layer, and the followed long-runout mobility depends
645 on topographic change and dissipated time of the pore water pressure.

646

647 **5. Conclusions**

648 The flowslide overridden on a liquified substrate generally mobilized on a nearly
649 flat flow path, causing rapid long-runout distance and catastrophic threats. We studied
650 the Saleshan landslide of Gansu in China, which is a typical loess flowslide mobilized
651 on the nearly flat terrace with an easily liquefied alluvial sand substrate. The
652 geomorphologic imprints and topographic changes present the different dynamic
653 features and mobilized behaviors at different zones of the Saleshan landslide. And its
654 accumulated features and the placemarks show that the landslide exists a motion
655 transformation from the slide on the steep slope to flow on the gentle terrace with
656 rapid velocity and long-runout distance. Meanwhile, ERT surveying confirms the
657 existence of abundant groundwater in the accumulation zone of the Saleshan landslide,
658 which is crucial to the motion transformation.

659 Our triaxial shear tests suggest that loess, alluvial sand, and red soil are sensitive
660 to liquefaction at the undrained conditions. Among them, the loess is the easiest
661 liquefaction. The impact loading test results show that the alluvial sand is natural
662 liquefaction at undrained condition while it is difficult to drained condition due to rapid
663 water pore pressure dissipation. This aggravated the occurrence of the mobilized loess.
664 As a result, the progress enhanced the mobilization of the Saleshan landslide on the
665 nearly flat terrace. Overall, we conclude that the hydrologic condition of the terrace is
666 essential to the movement of the Saleshan landslide, and the liquefaction features of
667 the materials are the key to its transformation during the landslide's movement.
668 Meanwhile, this kind of flowslide overridden on the liquified substrate partakes more

669 of mass transport than a mass movement.

670

671 **Acknowledgments**

672 This study was partially supported by the National Natural Science Foundation of
673 China (Nos. 41977212, 41790443 and 41927806), the National Key Research and
674 Development Program of China (No. 2018YFC504702). Mr. Xishan Lin, Mr. Shuaijun
675 Hu, and Mr. Xiaoming Feng of Lanzhou University are thanked for their help in the field
676 investigation. Yao Jiang acknowledges support from the CAS Pioneer Hundred Talents
677 Program. Images of the geographic, topographic, geomorphic maps and photographs
678 used for this paper are properly cited and referenced. Original data from ERT, particle
679 size distribution and triaxial shear test are available upon request
680 (zhangfy@lzu.edu.cn).

681

682 **References**

- 683 Aaron, J., Hungr, O., Stark, T.D., Baghdady, A.K., 2017. Oso, Washington, landslide of March 22, 2014:
684 Dynamic analysis. *Journal of Geotechnical & Geoenvironmental Engineering* 143.
- 685 Bogiatzis, P., 2015. Revitalizing decades-old analog seismograms through image analysis and digitization.
686 Mathwork, Technical Articles and Newsletters,
687 [https://www.mathworks.com/company/newsletters/articles/revitalizing-decades-old-analog-](https://www.mathworks.com/company/newsletters/articles/revitalizing-decades-old-analog-seismograms-through-image-analysis-and-digitization.html?s_tid=srchtitle)
688 [seismograms-through-image-analysis-and-digitization.html?s_tid=srchtitle](https://www.mathworks.com/company/newsletters/articles/revitalizing-decades-old-analog-seismograms-through-image-analysis-and-digitization.html?s_tid=srchtitle).
- 689 Burda, J., Veselý, M., Řehoř, M., Vilímek, V., 2018. Reconstruction of a large runout landslide in the
690 Krušné hory Mts. (Czech Republic). *Landslides* 15, 423–437.
- 691 Carraro, J.A.H., Prezzi, M., Salgado, R., 2009. Shear strength and stiffness of sands containing plastic or
692 nonplastic fines. *Journal of Geotechnical and Geoenvironmental Engineering* 135, 1167-1178.
- 693 Chambers, J., Meldrum, P., Gunn, D., Wilkinson, P., Merritt, A., Murphy, W., West, J., Kuras, O., Haslam,
694 E., Hobbs, P., 2013. Geophysical-geotechnical sensor networks for landslide monitoring. *Landslide*
695 *Science and Practice*. Springer, pp. 289-294.
- 696 Collins, B.D., Reid, M.E., 2020. Enhanced landslide mobility by basal liquefaction: The 2014 State Route
697 530 (Oso), Washington, landslide. *GSA Bulletin* 132, 451-476.
- 698 Crawford, M.M., Bryson, L.S., Woolery, E.W., Wang, Z., 2019. Long-term landslide monitoring using soil-

699 water relationships and electrical data to estimate suction stress. *Engineering Geology* 251, 146-157.

700 Crosta, G., Imposimato, S., Roddeman, D., 2009a. Numerical modeling of 2 - D granular step collapse
701 on erodible and nonerodible surface. *Journal of Geophysical Research: Earth Surface* 114.

702 Crosta, G.B., Blasio, F.V., Caro, M., Volpi, G., Imposimato, S., Roddeman, D., 2016. Modes of propagation
703 and deposition of granular flows onto an erodible substrate: experimental, analytical, and numerical
704 study. *Landslides*, 1-22.

705 Crosta, G.B., Blasio, F.V.D., Locatelli, M., Imposimato, S., Roddeman, D., 2015. Landslides falling onto a
706 shallow erodible substrate or water layer: an experimental and numerical approach. *IOP Conference
707 Series: Earth and Environmental Science* 26, 012004.

708 Crosta, G.B., Imposimato, S., Roddeman, D., 2009b. Numerical modelling of entrainment/deposition in
709 rock and debris-avalanches. *Engineering Geology* 109, 135-145.

710 Derbyshire, E., Meng, X.M., Dijkstra, T.A., 2000. *Landslides in the Thick Loess Terrain of North-West
711 China*. Wiley.

712 Dufresne, A., Geertsema, M., 2020. Rock slide–debris avalanches: flow transformation and hummock
713 formation, examples from British Columbia. *Landslides*, 1-18.

714 Evans, S.G., Hungr, O., Clague, J.J., 2001. Dynamics of the 1984 rock avalanche and associated distal
715 debris flow on Mount Cayley, British Columbia, Canada; implications for landslide hazard assessment
716 on dissected volcanoes. *Engineering Geology* 61, 29-51.

717 Grandjean, G., Gourry, J.C., Sanchez, O., Bitri, A., Garambois, S., 2011. Structural study of the Ballandaz
718 landslide (French Alps) using geophysical imagery. *Journal of Applied Geophysics* 75, 531-542.

719 Huang, R., 2009. Some catastrophic landslides since the twentieth century in the southwest of China.
720 *Landslides* 6, 69-81.

721 Hungr, O., Evans, S.G., 2004. Entrainment of debris in rock avalanches: An analysis of a long run-out
722 mechanism. *Geological Society of America Bulletin* 116, 1240-1252.

723 Hungr, O., Leroueil, S., Picarelli, L., 2014. The Varnes classification of landslide types, an update.
724 *Landslides* 11, 167-194.

725 Hutchinson, J.N., Bhandari, R.K., 1971. Undrained loading, a fundamental mechanism of mudflows and
726 other mass movements. *Géotechnique* 21, 353-358.

727 Ishihara, K., Okusa, S., Oyagi, N., Ischuk, A., 1990. Liquefaction-induced flowslide in the collapsible loess
728 deposit in Soviet Tajik. *Soils and Foundations* 30, 73-89.

729 Iverson, R.M., George, D.L., 2016. Modelling landslide liquefaction, mobility bifurcation and the
730 dynamics of the 2014 Oso disaster. *Géotechnique* 66, 175-187.

731 Iverson, R.M., George, D.L., Allstadt, K., Reid, M.E., Collins, B.D., Vallance, J.W., Schilling, S.P., Godt, J.W.,
732 Cannon, C.M., Magirl, C.S., Baum, R.L., Coe, J.A., Schulz, W.H., Bower, J.B., 2015. Landslide mobility and
733 hazards: implications of the 2014 Oso disaster. *Earth and Planetary Science Letters* 412, 197-208.

734 Iverson, R.M., Reid, M.E., LaHusen, R.G., 1997. Debris-flow mobilization from landslides. *Annual Review
735 of Earth and Planetary Sciences* 25, 85-138.

736 Iverson, R.M., Reid, M.E., Logan, M., LaHusen, R.G., Godt, J.W., Griswold, J.P., 2011. Positive feedback
737 and momentum growth during debris-flow entrainment of wet bed sediment. *Nature Geoscience* 4,
738 116-121.

739 Kang, C., Zhang, F., Pan, F., Peng, J., Wu, W., 2018. Characteristics and dynamic runout analyses of 1983
740 Saleshan landslide. *Engineering Geology* 234, 181-195.

741 Kramer, S.L., 1988. Triggering of liquefaction flow slides in coastal soil deposits. *Engineering Geology* 26,
742 17-31.

743 Li, P., Shen, W., Hou, X., Li, T., 2019. Numerical simulation of the propagation process of a rapid flow-like
744 landslide considering bed entrainment: A case study. *Engineering Geology* 263, 105287.

745 Ma, J., Qian, J., 1998. Prediction and evaluation of the influence on environmental hydrogeology in
746 nalesi irrigation district of Baxiehe River Basin. *Journal of Lanzhou University* 34, 106-111.

747 Mangeney, A., 2011. Landslide boost from entrainment. *Nature Geoscience* 4, 77-78.

748 Miao, T., Liu, Z., Niu, Y., Ma, C., 2001. A sliding block model for the runout prediction of high-speed
749 landslides. *Canadian Geotechnical Journal* 38, 217-226.

750 Misfeldt, G.A., Sauer, E.K., Christiansen, E.A., 1991. The Hepburn landslide: an interactive slope-stability
751 and seepage analysis. *Canadian Geotechnical Journal* 28, 556-573.

752 Paguican, E.M.R., Wyk de Vries, B., Lagmay, A.M.F., 2014. Hummocks: how they form and how they
753 evolve in rockslide-debris avalanches. *Landslides* 11, 67-80.

754 Pavoni, N., 1968. Über die Entstehung der Kiesmassen im Bergsturzgebiet von Bonaduz-Reichenau
755 (Graubünden). *Eclogae Geol. Helv* 61/2, 494-500.

756 Peng, D., Xu, Q., Zhang, X., Xing, H., Zhang, S., Kang, K., Qi, X., Ju, Y., Zhao, K., 2019. Hydrological response
757 of loess slopes with reference to widespread landslide events in the Heifangtai terrace, NW China.
758 *Journal of Asian Earth Sciences* 171, 259-276.

759 Peng, J., Fan, Z., Wu, D., Zhuang, J., Dai, F., Chen, W., Zhao, C., 2015. Heavy rainfall triggered loess-
760 mudstone landslide and subsequent debris flow in Tianshui, China. *Engineering Geology* 186, 79-90.

761 Peng, J., Ma, P., Wang, Q., Zhu, X., Zhang, F., Tong, X., Huang, W., 2018. Interaction between landsliding
762 materials and the underlying erodible bed in a loess flowslide. *Engineering Geology* 234, 38-49.

763 Peng, J., Wang, G., Wang, Q., Zhang, F., 2017a. Shear wave velocity imaging of landslide debris deposited
764 on an erodible bed and possible movement mechanism for a loess landslide in Jingyang, Xi'an, China.
765 *Landslides* 14, 1503-1512.

766 Peng, J., Zhang, F., Wang, G., 2017b. Rapid loess flow slides in Heifangtai terrace, Gansu, China.
767 *Quarterly Journal of Engineering Geology and Hydrogeology* 50, 106-110.

768 Perrone, A., Lapenna, V., Piscitelli, S., 2014. Electrical resistivity tomography technique for landslide
769 investigation: A review. *Earth-Science Reviews* 135, 65-82.

770 Picarelli, L., 2010. Discussion on "A rapid loess flowslide triggered by irrigation in China". *Landslides* 7,
771 203-205.

772 Poschinger, A.v., Kippel, T., 2009. Alluvial deposits liquefied by the Flims rock slide. *Geomorphology* 103,
773 50-56.

774 Sassa, K., Wang, G., 2005. Mechanism of landslide-triggered debris flows: Liquefaction phenomena due
775 to the undrained loading of torrent deposits. *Debris-flow hazards and related phenomena*. Springer, pp.
776 81-104.

777 Stark, T.D., Baghdady, A.K., Hungr, O., Aaron, J., 2017. Case Study: Oso, Washington, Landslide of March
778 22, 2014—Material Properties and Failure Mechanism. *Journal of Geotechnical and Geoenvironmental*
779 *Engineering*, 05017001.

780 Sun, D., Bloemendal, J., Rea, D.K., Vandenberghe, J., Jiang, F., An, Z., Su, R., 2002. Grain-size distribution
781 function of polymodal sediments in hydraulic and aeolian environments, and numerical partitioning of
782 the sedimentary components. *Sedimentary Geology* 152, 263-277.

783 Taira, A., Scholle, P.A., 1979. Origin of bimodal sands in some modern environments. *Journal of*
784 *Sedimentary Research* 49, 777-786.

785 Take, W.A., Beddoe, R.A., 2014. Base liquefaction: a mechanism for shear-induced failure of loose
786 granular slopes. *Canadian Geotechnical Journal*, 496-507.

787 Wang, G., Huang, R., Chigira, M., Wu, X., Lourenço, S.D.N., 2013. Landslide amplification by liquefaction
788 of runout-path material after the 2008 Wenchuan (M 8.0) Earthquake, China. *Earth Surface Processes
789 and Landforms* 38, 265-274.

790 Wang, G., Sassa, K., Fukuoka, H., 2003. Downslope volume enlargement of a debris slide-debris flow in
791 the 1999 Hiroshima, Japan, rainstorm. *Engineering Geology* 69, 309-330.

792 Wang, G., Sassa, K., Fukuoka, H., Tada, T., 2007. Experimental study on the shearing behavior of
793 saturated silty soils based on ring-shear tests. *Journal of Geotechnical and Geoenvironmental
794 Engineering* 133, 319-333.

795 Wang, G., Zhang, D., Furuya, G., Yang, J., 2014. Pore-pressure generation and fluidization in a loess
796 landslide triggered by the 1920 Haiyuan earthquake, China: A case study. *Engineering Geology* 174, 36-
797 45.

798 Wang, S., Zhang, Z., Zhan, Z., Liu, H., 1988. On the characteristics and dynamics of the catastrophic
799 Mount Sale landslide, Gansu. *Journal Chengdu College of Geology* 15, 58-63.

800 Wartman, J., Montgomery, D.R., Anderson, S.A., Keaton, J.R., Benoît, J., dela Chapelle, J., Gilbert, R.,
801 2016. The 22 March 2014 Oso landslide, Washington, USA. *Geomorphology* 253, 275-288.

802 Wheaton, J.M., Brasington, J., Darby, S.E., Sear, D.A., 2010. Accounting for uncertainty in DEMs from
803 repeat topographic surveys: improved sediment budgets. *Earth Surface Processes and Landforms* 35,
804 136-156.

805 Wheaton, J.M., Fryirs, K.A., Brierley, G., Bangen, S.G., Bouwes, N., O'Brien, G., 2015. Geomorphic
806 mapping and taxonomy of fluvial landforms. *Geomorphology* 248, 273-295.

807 Wilkinson, P., Chambers, J., Uhlemann, S., Meldrum, P., Smith, A., Dixon, N., Loke, M.H., 2016.
808 Reconstruction of landslide movements by inversion of 4-D electrical resistivity tomography monitoring
809 data. *Geophysical Research Letters* 43, 1166-1174.

810 Wu, W., Wang, N., 2006. *Landslide hazards in Gansu*. Lanzhou University Press, Gansu, China.

811 Xu, L., Dai, F., Kwong, A., Tham, L., Tu, X., 2009. Analysis of some special engineering-geological problems
812 of loess landslide. *Chinese Journal of Geotechnical Engineering* 31, 287-293.

813 Zhang, F., Kang, C., Chan, D., Zhang, X., Pei, X., Peng, J., 2017. A study of a flowslide with significant
814 entrainment in loess areas in China. *Earth Surface Processes and Landforms* 42, 2295-2305.

815 Zhang, F., Wang, G., 2018. Effect of irrigation-induced densification on the post-failure behavior of loess
816 flowslides occurring on the Heifangtai area, Gansu, China. *Engineering Geology* 236, 111-118.

817 Zhang, F., Wang, G., Kamai, T., Chen, W., 2014. Effect of pore water chemistry on undrained shear
818 behaviour of saturated loess. *Quarterly Journal of Engineering Geology and Hydrogeology* 47, 201-210.

819 Zhang, F., Wang, G., Kamai, T., Chen, W., Zhang, D., Yang, J., 2013. Undrained shear behavior of saturated
820 loess with different concentrations of sodium chlorate solution. *Engineering Geology* 155, 69-79.

821 Zhang, F., Yan, B., Feng, X., Lan, H., Kang, C., Lin, X., Zhu, X., Ma, W., 2019. A rapid loess mudflow
822 triggered by the check dam failure in a bulldoze mountain area, Lanzhou, China. *Landslides* 16, 1981-
823 1992.

824 Zhang, Z., Chen, S., Tao, L., 2002. 1983 Sale Mountain landslide, Gansu Province, China. *Reviews in
825 Engineering Geology* 15, 149-164.

826 Zhang, Z., Wang, S., 1984. On the prediction of the occurrence time and the velocity of a potential
827 landslide. *Proceedings, 4th International Symposium on Landslides, Toronto, Canada*, pp. 145-146.

828 Zhuang, J., Peng, J., 2014. A coupled slope cutting—a prolonged rainfall-induced loess landslide: a 17
829 October 2011 case study. *Bulletin of Engineering Geology and the Environment* 73, 997-1011.

830 **Figure captions**

831 Fig. 1 Geographical location and reviews of the Saleshan landslide. (a) Location of the
832 Saleshan landslide in Gansu Province, China; (b) Landslide inventory of Baxie River
833 catchment; (c) Panoramic photograph of the Saleshan landslide in 1983 (Courtesy of Y.
834 Wang); (d) Panoramic photograph of the Saleshan landslide in 2015.

835 Fig. 2 Simplified stratigraphic and topographic section of the Saleshan landslide. (a)
836 Before slope failure; (b) After slope failure.

837 Fig. 3 Geomorphologic map of Saleshan landslide. 1 Depletion zone; 2 Accumulation
838 zone 3 Depressions; 4 Hillocks; 5 Grooves; 6 Hummocks; 7 Main scarp; 8 Minor scarp;
839 9 Crown cracks; 10 Lateral cracks; 11 Transverse cracks; 12 Radial cracks; 13 Flanks; 14
840 Contour lines; 15 Gullies; 16 Springs; 17 Baxie River; 18 Jiuer reservoir. The boxes
841 indicate photo locations in Fig. 4, respectively.

842 Fig. 4 Photographs illustrating typical geomorphological imprints of Saleshan landslide
843 in 1983. (a) Sub-vertical main scarp; (b) Head scarp with depression and hillock; (c)
844 Standing cow in accumulation zone; (d) Life-saving tree at the toe (photo from Zhang
845 *et al.*, 2002); (e) Lateral cracks on the east-side at left flank; (f) Transverse cracks on
846 the west-side at right flank; (g) Transverse cracks on the east-side at left flank; (h)
847 Radial cracks at the toe; (i) Loess liquefaction at right flank on accumulation zone; (j)
848 landslide deposition and dammed lake in Baxie River; (k) Buried Jiuer reservoir and
849 transverse cracks; (l) incompletely liquefied loess on the east-side accumulation zone.

850 See Fig. 3 for photo locations.

851 Fig. 5 Topographic change detection of pre- and post landslide of the Saleshan

852 landslide. (a) The elevation difference map; (b) the areal change distribution; and (c)
853 the volumetric elevation change distribution. Black lines indicate the profile locations
854 in Fig. 6, and red lines show the profile locations of the ERT surveying in Fig. 8.

855 Fig. 6 The topographic changes of alternative profiles of the Saleshan landslide, and
856 the specified locations see Fig. 5.

857 Fig. 7 Motion displacement vector at different placemark locations on the Saleshan
858 landslide. 1 Depletion zone; 2 West accumulation zone; 3 Central accumulation zone;
859 4 East accumulation zone; 5 House location before failure; 6 House location after
860 failure; 7 Ground marks before failure; 8 Ground marks after failure; 9 Tree location
861 before and after failure; 10 Life-saving tree before and after failure; 11 Placemark
862 number.

863 Fig. 8 Interpreted Wenner ERT sections of four profiles on the Saleshan landslide. Note:
864 the dashed lines are derived from the real topographic profile, and the detailed
865 locations see Fig. 5 and Fig. 6.

866 Fig. 9 The exemplified particle size distribution of the three types of soils on the
867 Saleshan landslide. (a) Cumulative distribution curves of particle size; (b) Frequent
868 distribution curves of particle size.

869 Fig. 10 Undrained triaxial test results of the three different specimens at same
870 confining pressures. (a) Deviator stress versus axial strain; (b) Pore water pressure
871 versus axial strain; (c) Effective stress path

872 Fig. 11 Undrained triaxial test results of the alluvial sand specimens at different
873 confining pressures. (a) Deviator stress versus axial strain; (b) Pore water pressure

874 versus axial strain; (c) Effective stress path

875 Fig. 12 Triaxial test results from quasi-dynamic impact stress loading of the alluvial
876 sand specimens. (a) drained impact loading condition; (b) undrained impact loading
877 condition.

878 Fig. 13 Hypothesised sequence from progressive deformation to the catastrophic
879 mobility of the Saleshan landslide.

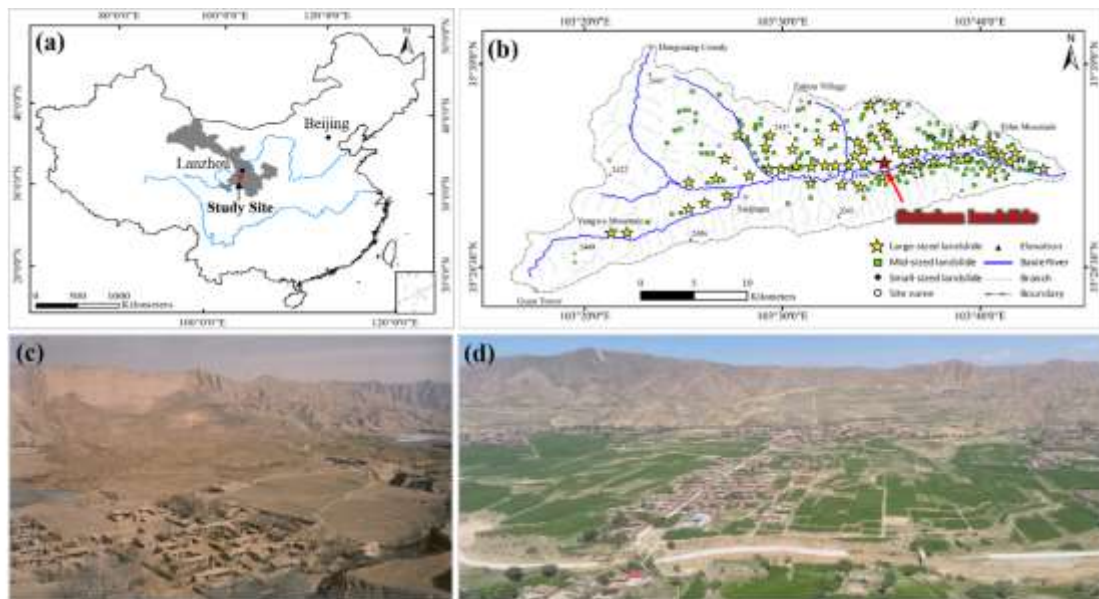
880 Fig. 14 Schematic illustration of two types of entrainment. (a) Mobility overridden on
881 the liquefied substrate on nearly flat flow path; (b) Mobility eroded the liquefied layer
882 in relatively steep channel flow path.

883

884

885 Fig. 1

886

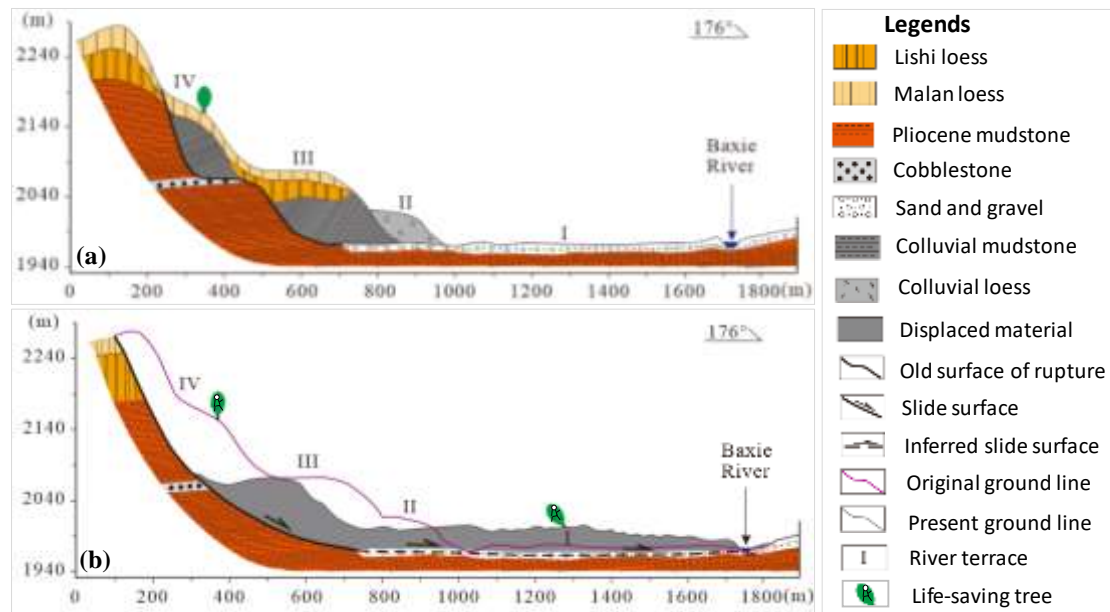


887

888

889 Fig. 2

890

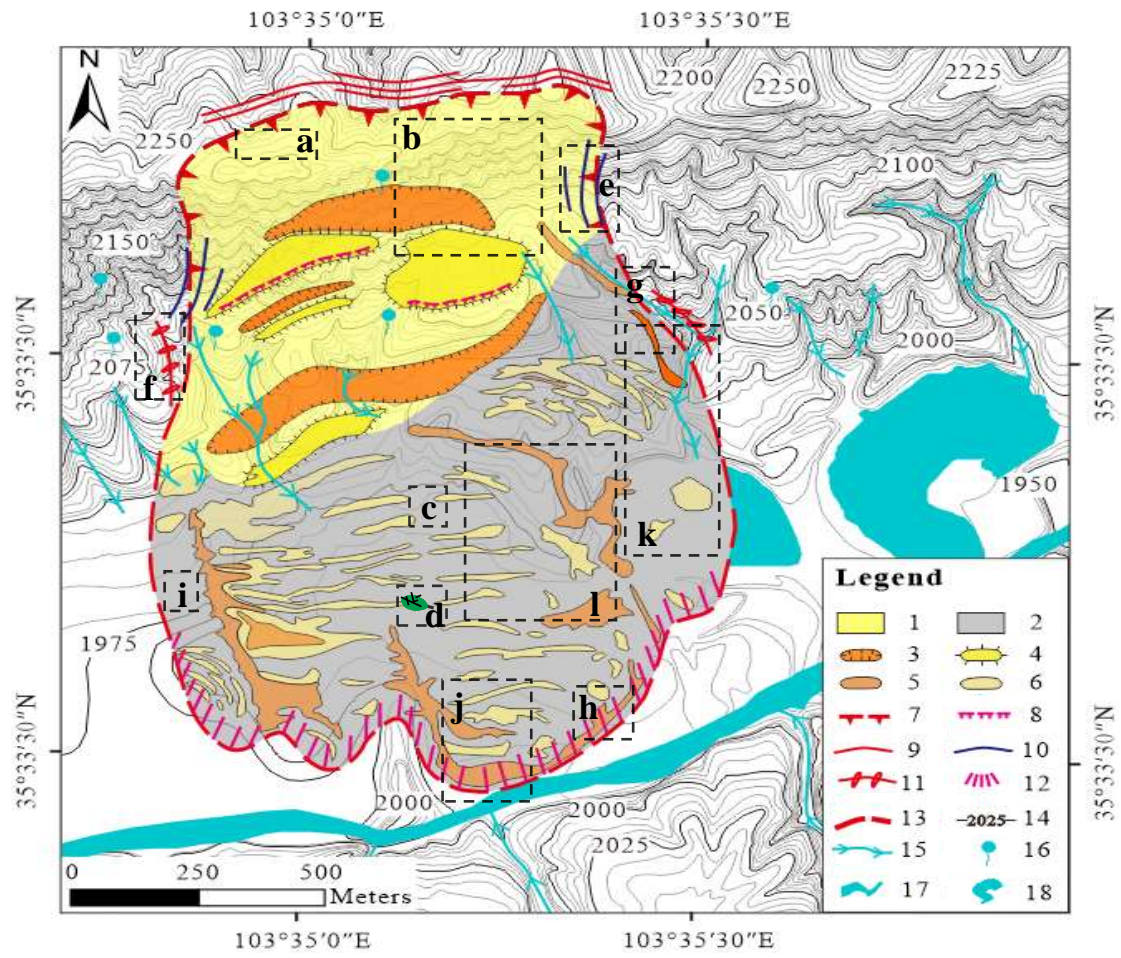


891

892

893
894
895

Fig. 3

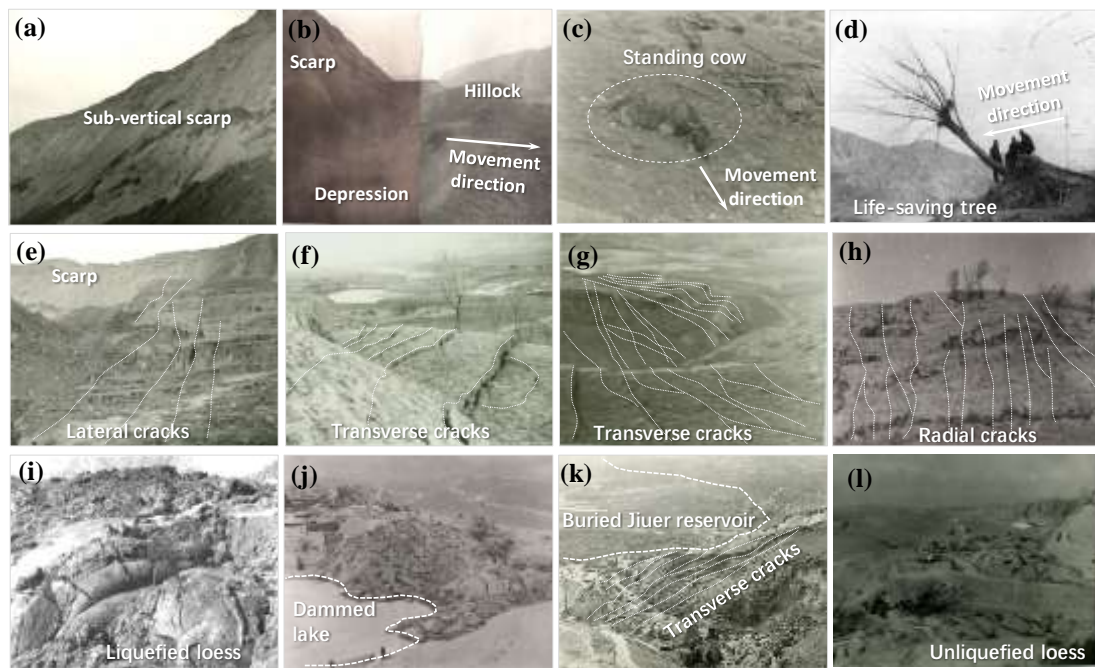


896
897

898

899 Fig. 4

900

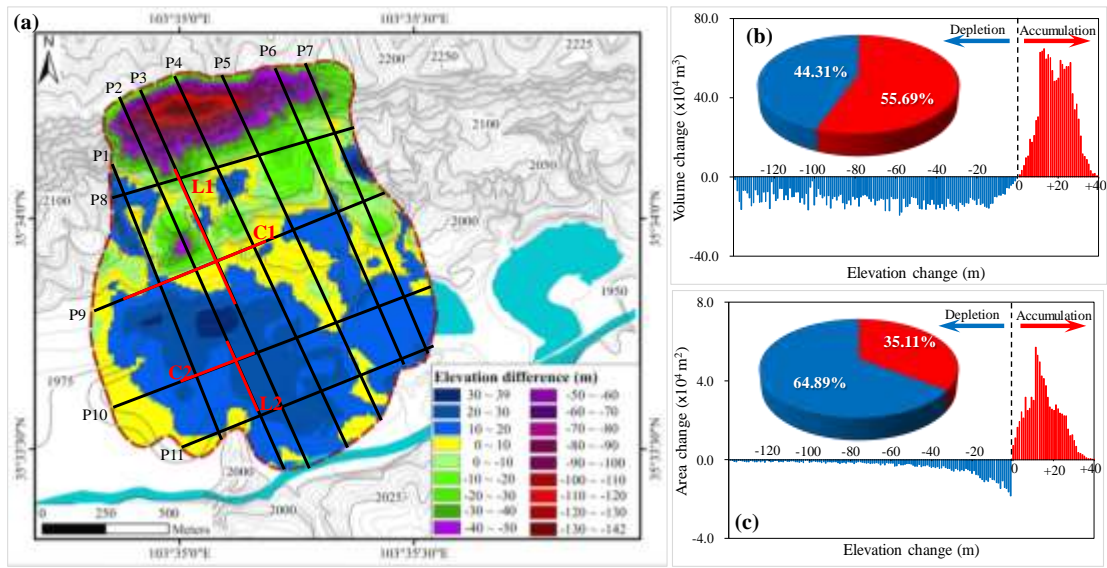


901

902

903
904
905

Fig. 5

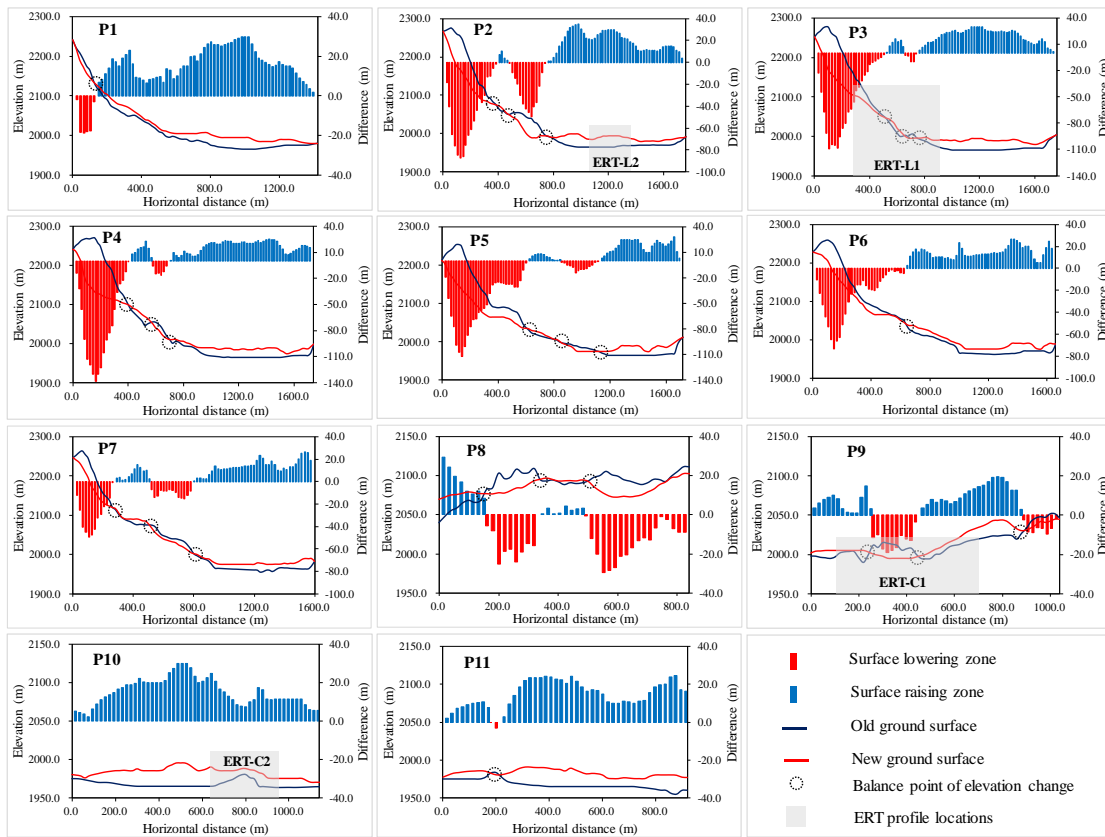


906
907

908

909 Fig. 6

910



911

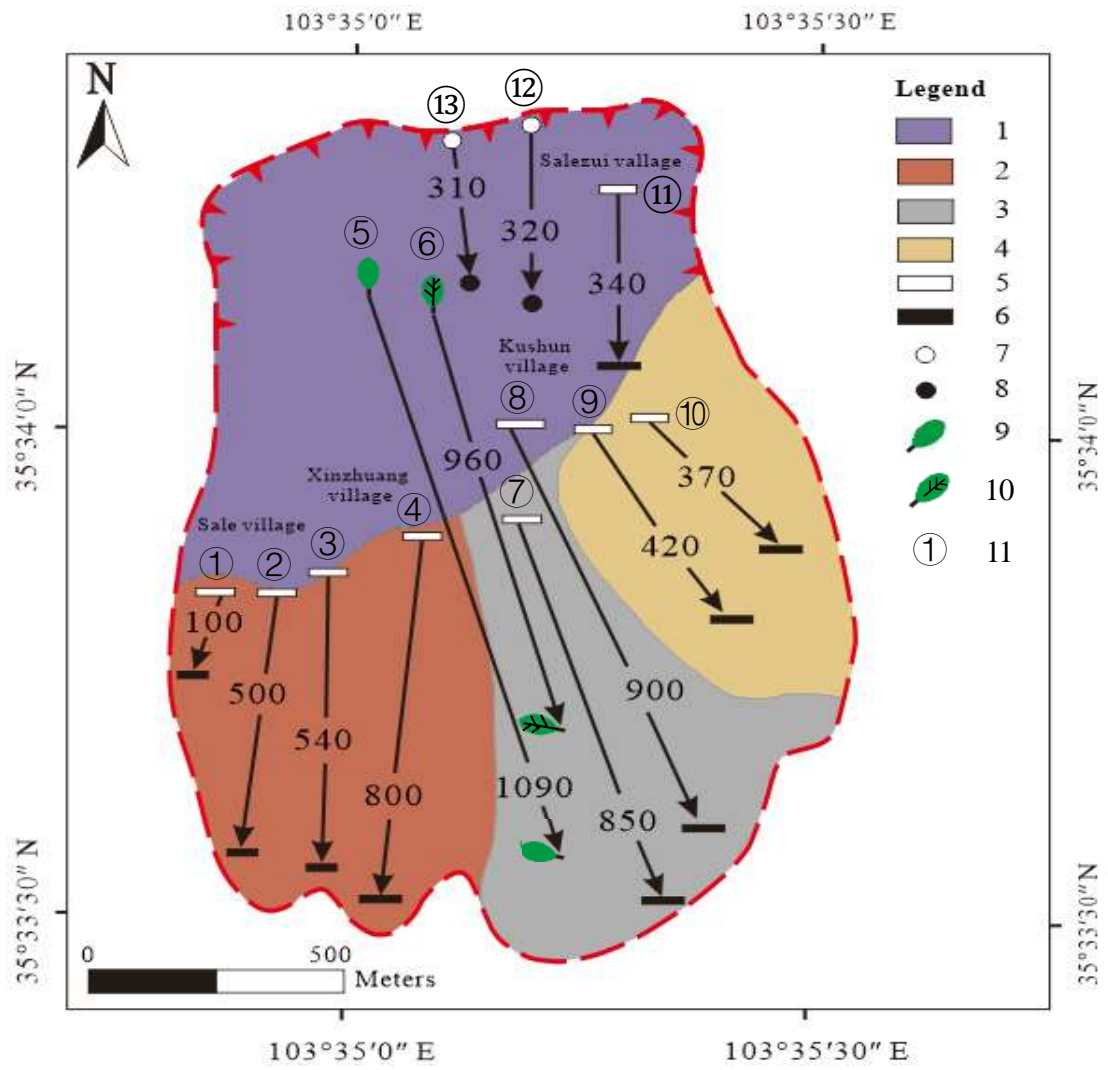
912

913

914

915 Fig. 7

916

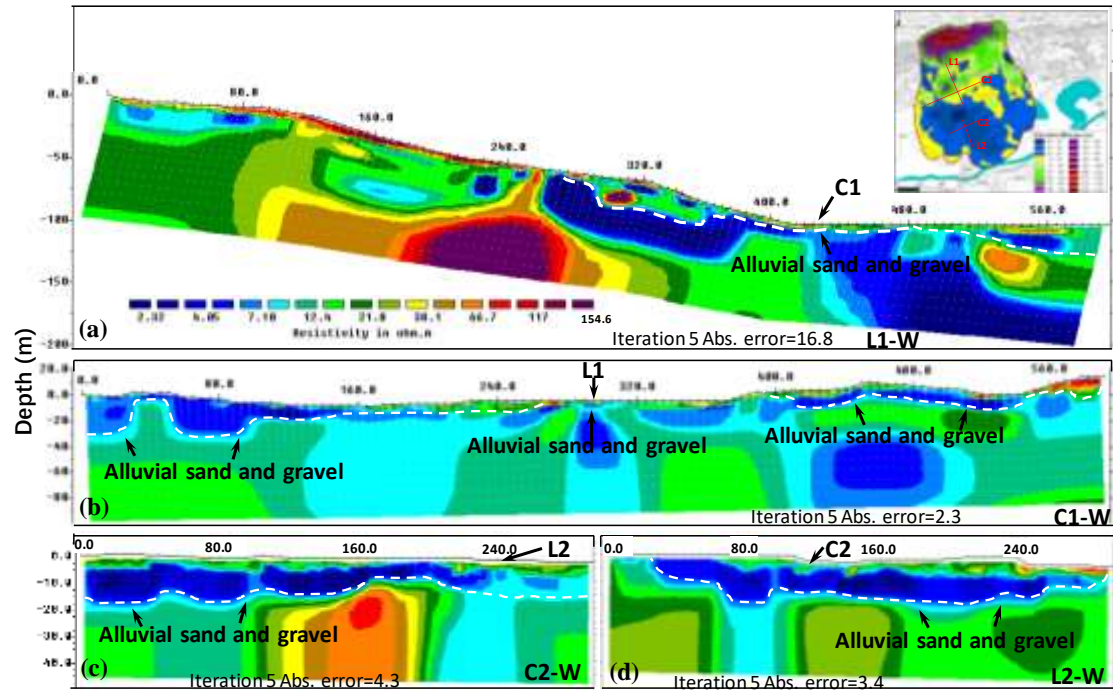


917

918

919
920
921

Fig. 8

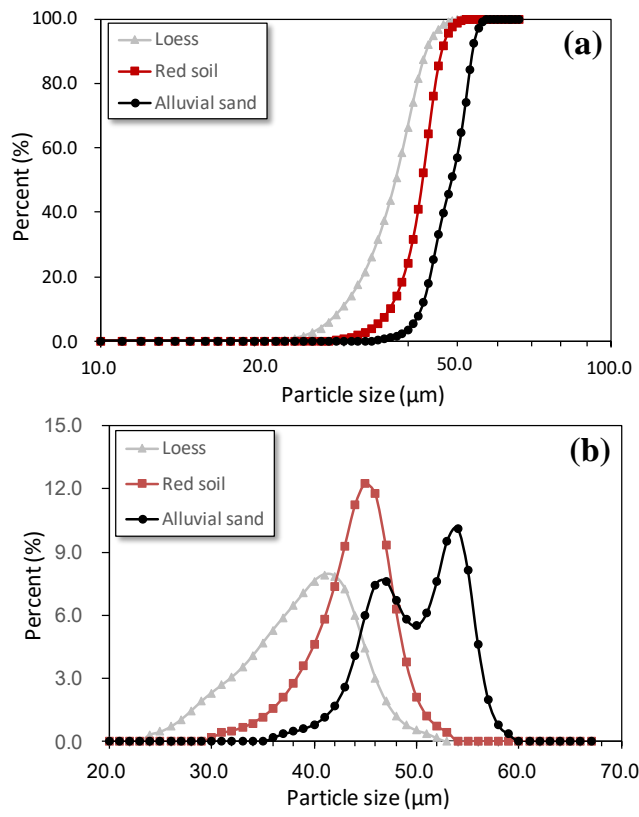


922
923

924

925 Fig. 9

926



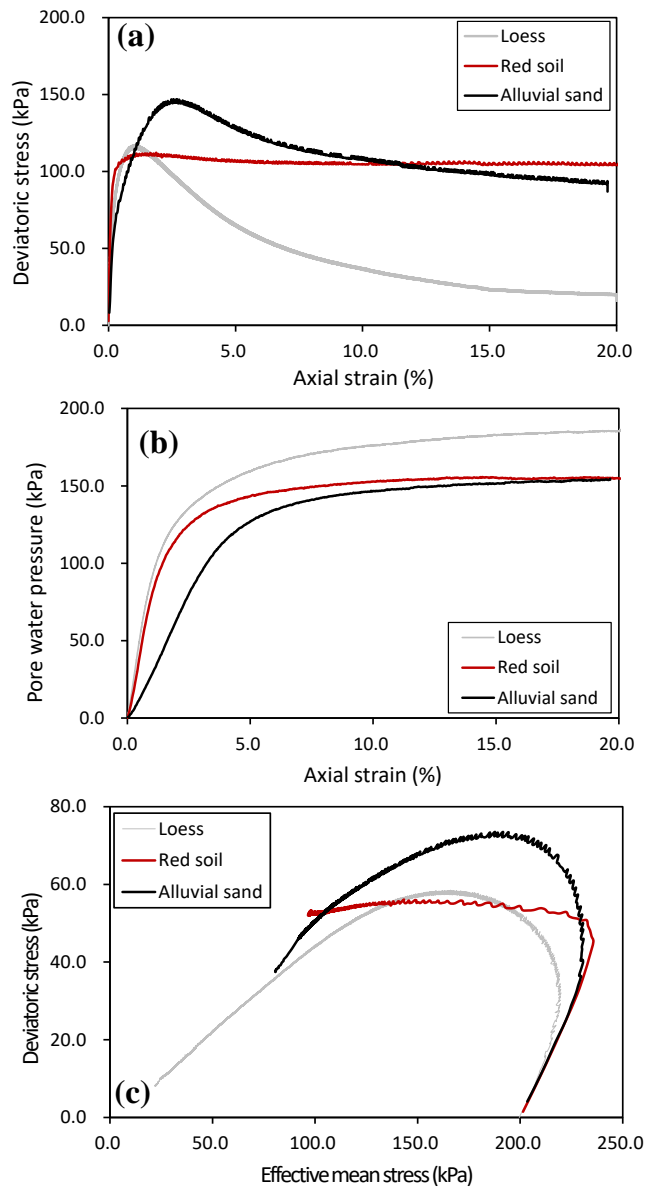
927

928

929

930 Fig. 10

931

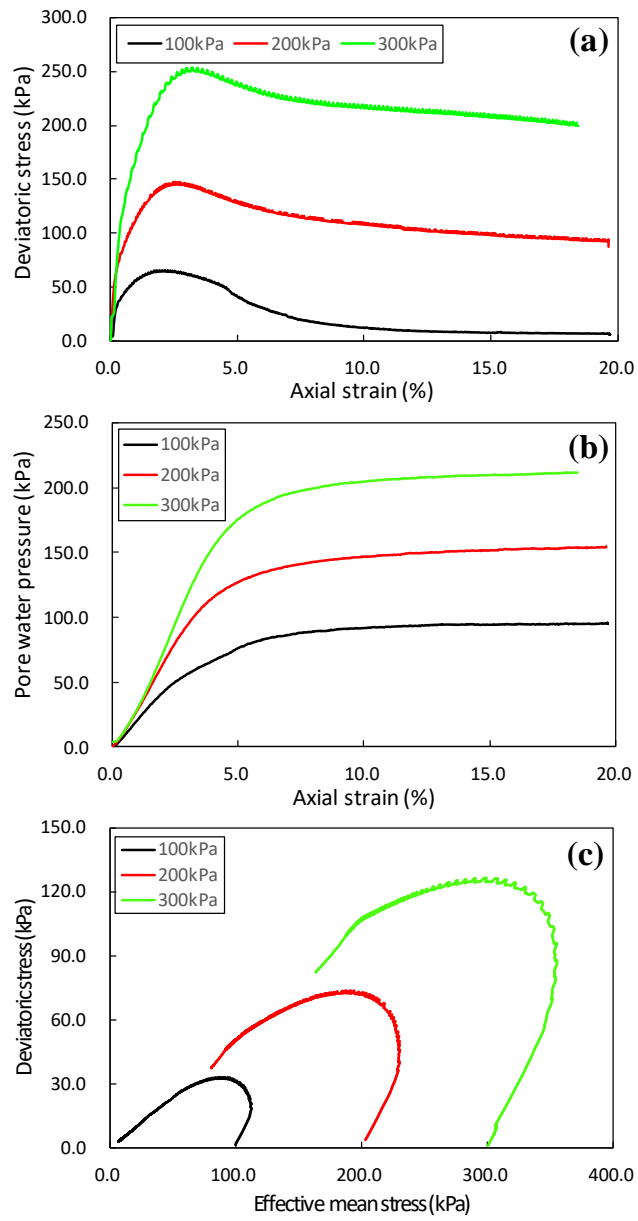


932

933

934
935
936

Fig. 11

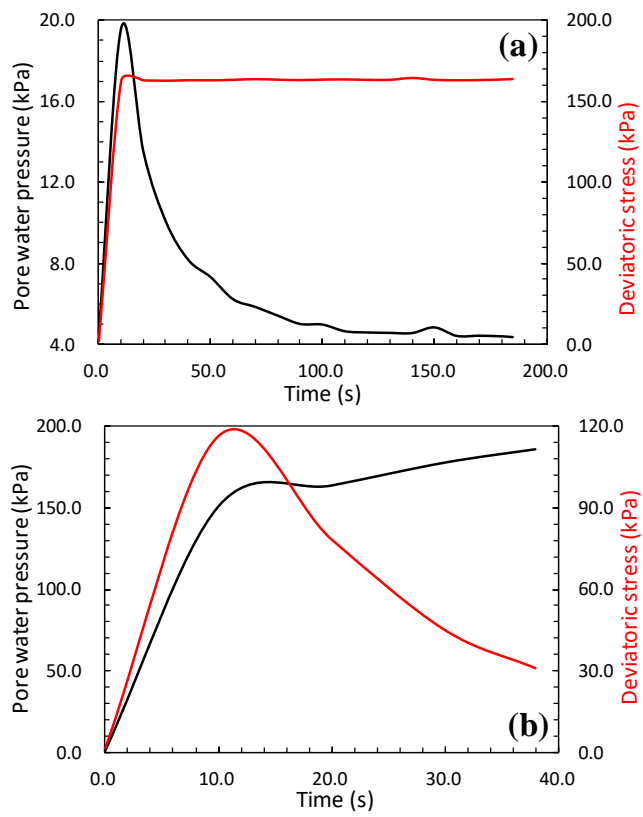


937
938

939

940 Fig. 12

941

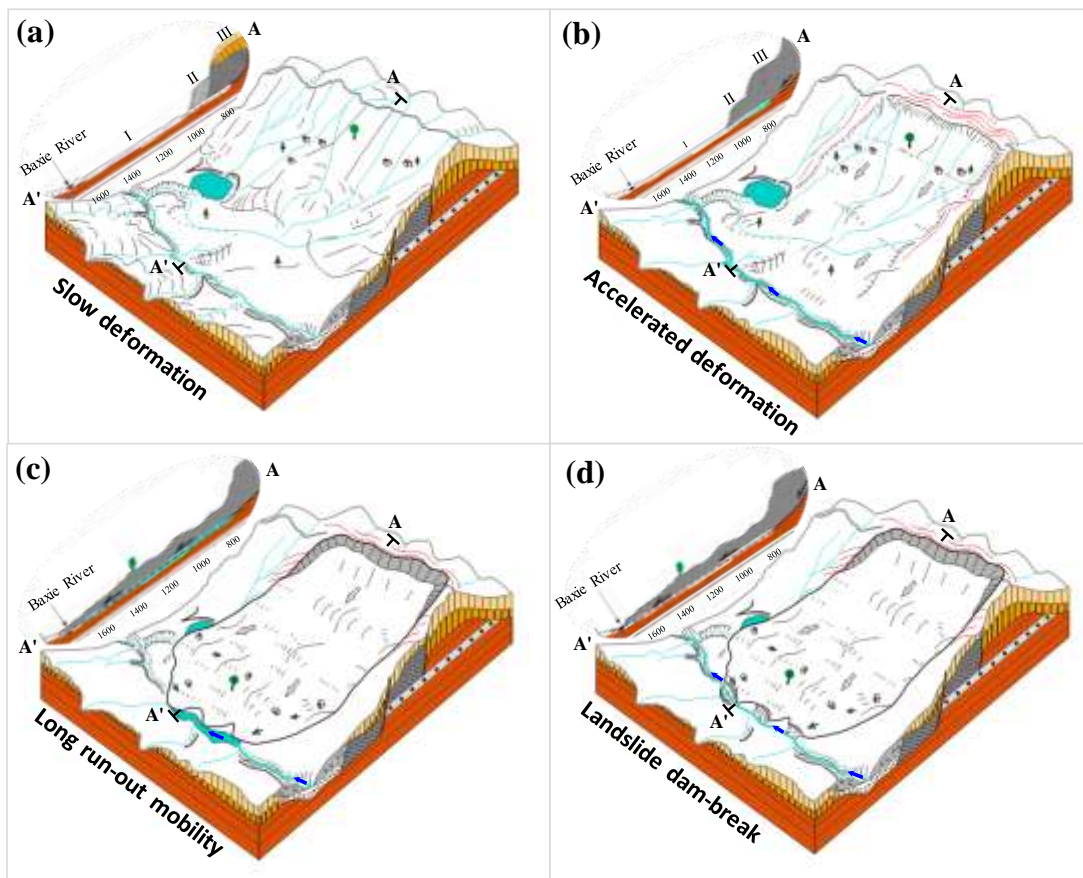


942

943

944

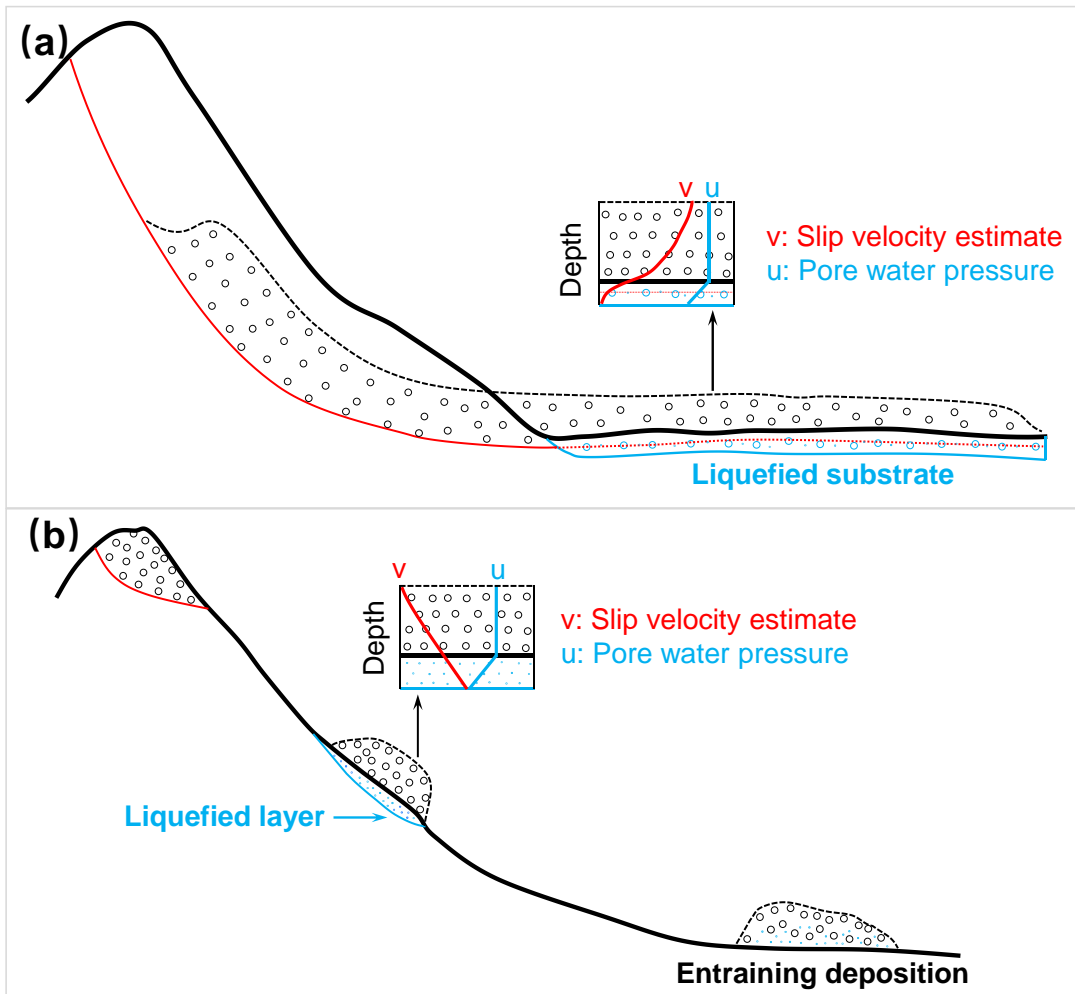
945 Fig. 13



946

947
948
949

Fig. 14



950

951

952 Table 1: Kinematic parameters of different placemark locations on the Saleshan
953 landslide

No.	PL	TD (°)	HD (m)	V (m/s)	AV (m/s)
1		195	100	1.8	
2	WAZ	187	500	9.1	8.8
3		183	540	9.8	
4		188	800	14.5	
5		167	1090	19.8	
6	CAZ	173	960	17.5	16.7
7		170	850	15.5	
8		166	900	16.4	
9	EAZ	150	420	7.6	7.2
10		149	370	6.7	
11		179	340	6.2	
12	DZ	180	320	5.8	5.9
13		175	310	5.6	

954 Note, No.: Placemark number; PL: Placemark location; TD: Travel direction; HD:
955 Horizontal displacement; V: Velocity; AV: Average velocity; WAZ: West accumulation
956 zone; CAZ: Central accumulation zone; EAZ: East accumulation zone; DZ: Depletion
957 zone.